Measurement of transformation temperatures and specific heat capacity of tungsten added reduced activation ferritic–martensitic steel

S. Raju *, B. Jeya Ganesh, Arun Kumar Rai, R. Mythili, S. Saroja, E. Mohandas, M. Vijayalakshmi, K.B.S. Rao, Baldev Raj

Indira Gandhi Centre for Atomic Research (IGCAR), Physical Metallurgy Division, Kalpakkam, Tamil Nadu 603 102, India

ARTICLE INFO

ABSTRACT

The on-heating phase transformation temperatures up to the melting regime and the specific heat capacity of a reduced activation ferritic–martensitic steel (RAFM) with a nominal composition (wt%): 9Cr–0.09C–0.56Mn–0.23V–1W–0.063Ta–0.02N, have been measured using high temperature differential scanning calorimetry. The α-ferrite + carbides $\rightarrow$ γ-austenite transformation start and finish temperatures, namely Ac_1, and Ac_3, are found to be 1104 and 1144 K, respectively for a typical normalized and tempered microstructure. It is also observed that the martensite start (M_S) and finish (M_f) temperatures are sensitive to the austenitising conditions. Typical M_S and M_f values for the 1273 K normalized and 1033 K tempered samples are of the order 714 and 614 K, respectively. The heat capacity C_P of the RAFM steel has been measured in the temperature range 473–1273 K, for different normalized and tempered samples. In essence, it is found that the C_P of the fully martensitic microstructure is found to be lower than that of its tempered counterpart, and this difference begins to increase in an appreciable manner from about 800 K. The heat capacity of the normalized microstructure is found to vary from 480 to 500 J kg^{-1} K^{-1} at 500 K, where as that of the tempered steel is found to be higher by about, 150 J kg^{-1} K^{-1}.

© 2009 Elsevier B.V. All rights reserved.

1. Introduction

It is well-known that low carbon medium to highly alloyed ferritic steels, especially the 9–10 wt% Cr ferritic–martensitic steels, constitute one of the major class of structural materials in fossil fuel based conventional power reactors and also in certain advanced liquid metal cooled nuclear fast reactors employing metallic fuel [1–5]. Besides some of these alloys are under consideration for certain nuclear fusion related applications. These alloys are generally known for their good oxidation resistance, high temperature creep-rupture strength, good thermal fatigue tolerance, adequate fracture toughness under typical service conditions and a fair degree of weldability [5]. Besides, they also possess good thermal conductivity, low thermal expansion characteristics when compared with austenitic grades and high swelling resistance to fast neutrons [5]. These properties render them the preferred candidate material for fission and fusion reactor applications [6]. While conventional ferritic–martensitic steels designed around 9Cr–1Mo composition have met with almost all the requirements that are stipulated for the in-pile applications in liquid metal cooled fast reactors, the emerging imperatives to develop fusion power have called for the development of newer grades, which can withstand neutron irradiation of higher energy and besides pose a compara-

tively reduced hazard from the induced radioactivity arising from transmuted transition elements. This latter requirement on the part of fusion reactor materials has catalyzed an extensive research and development program world wide on what are known as low or reduced activation ferritic–martensitic steels (RAFM) [3,4,7].

The guiding metallurgical principles for the design of RAFM steels are essentially the same as that of conventional high chromium low carbon alloys, such as P91/T91; but with one important caveat that elements producing long half-life transmutants like Ni, Mo, Nb, Cu, Co, Al, N, etc., are largely substituted by their comparatively low activation counterparts, such as Mn, W, V, Ta, and C, so that the RAFM steel at the end of its useful lifespan can be safely handled after a cooling period of about 100 years, rather than 1000 years, which would have been the case with conventional Cr–Mo–Ni–Nb containing ferritic steels [3,7]. It must be added that quite recently, Klueh has argued for the development of boron added newer modifications of RAFM steels from the point of view of improving its creep-rupture strength to levels that are realized in the standard Nb-added modified 9Cr steels [7].

The advent of RAFM steels has ushered in a spurt of interdisciplinary research activities aimed at gathering a comprehensive understanding of relevant physical, metallurgical and mechanical properties [12–27]. In India, an elaborate research program on the development and characterization of RAFM steels has been initiated recently. As a first step, a RAFM steel with a nominal composition (wt%) of 9Cr–0.09C–0.56Mn–0.23V–1W–0.063Ta–0.02N

* Corresponding author. Tel.: +91 44 274 80 306; fax: +91 44 274 80 081.
E-mail address: sraju@igcar.gov.in (S. Raju).

Table 1
The chemical composition in weight percent of the reduced activation ferritic–martensitic (RAFM) steel used in this study.

Steel designation	C	Cr	Mo	Mn	Si	V	Al	Ni	P	Co	Cu	S	N	W	Ti	Nb	Ta
Reduced activation steel	0.091	9.05	0.0036	0.56	0.05	0.226	0.0036	–	–	0.0043	0.005	–	0.0206	1.0	0.0024	0.0039	0.063

(see, Table 1) has been produced at MIDHANI. As a part of the characterization of this first melt, it was decided to make accurate measurements of the phase transformation temperatures and specific heat capacity of this indigenous RAFM steel, as reliable values for these material physical properties are required in enabling the knowledge based design of heat treatment and fabrication schedules. Accordingly, a high temperature differential scanning calorimetry (DSC) study has been carried out to investigate the high temperature phase stability and heat capacity behaviour of this steel. The results of this study are reported in this paper.

2. Experimental procedure

2.1. Alloy composition and heat treatment details

The RAFM steel used in this study is supplied by MIDHANI, Hyderabad, India. Its composition is listed in Table 1. The alloy was produced by vacuum induction melting followed by vacuum arc refining. In order to minimise the quantum of tramp elements, fairly pure constituents were used in alloy melting. The alloy had been remelted three or four times to ensure a high degree of homogeneity. The master ingot weighing about 300 kg had subsequently been hot forged into plates of 25 mm thickness. A small representative section of the hot forged ingot was taken up for characterization studies. Specimen of dimensions $10 \times 10 \times 5$ mm have been sliced from the plate for individual heat treatments and subsequent thermal stability and thermal property measurement studies.

Since ferritic steels are known to exhibit diverse microstructural features that are in direct relation to the heat treatments adopted, certain typical normalizing temperatures are chosen in the current investigation. These were followed by suitable tempering schedules to produce the standard normalized and tempered microstructures that are characteristic of 9Cr-ferritic alloys [28]. The various heat treatments given to RAFM steel are summarized in Table 2.

The choice of the solution treatment temperatures higher than about 1253 K is made in order to realize the full dissolution of $M_{23}C_6$ type carbides and to enhance the possible growth of austenite grains at high temperatures, which would promote the ease of formation of martensite upon subsequent air cooling. Although 9Cr – steels are generally known to be airhardenable, few samples were also quenched in water. As a preliminary remark, it may be

added that normalization treatments at 1253 and 1453 K resulted in near 100% martensite, while the ones quenched from 1553 K contained about 20% delta ferrite. For heat capacity measurements, we have taken the steel normalized at 1253 K, which were given a tempering treatment subsequently at 1033 K for various time durations. The relevant heat treatment details together with specimen designations are listed in Table 2.

2.2. Microstructural characterization

For basic metallographic characterization, the samples were ground and polished in the standard manner. The polished samples were given a mild initial etching with 2% nital to reveal the prior austenite grain boundaries and this was followed by a second etch with Villella's reagent to reveal the normalized and tempered microstructure. The optical microscopy was done using *Leica* MeF4A, and the microhardness measurements were made using *Leitz* microhardness tester, under a load of 100 g. A total of eight hardness readings were recorded and the average Vickers hardness number (VHN) is reported here. In Table 3, the heat treatment details and corresponding microhardness values are listed (see Table 3).

2.3. Differential scanning calorimetry (DSC) experiments

2.3.1. Transformation temperature measurements
The samples for DSC experiments were cut from the heat-treated plate using diamond coated wire saw. These were cleaned

Table 2
Heat treatment details adopted in this study.

S. No.	Treatment	Temperature/K	Time/h	Cooling method	Designation
1	As received state	Hot forged condition			As received
2	Solution treatment	1253	2	Air cooling (AC)	N-1253
3		1453	2	AC	N-1453
4		1453	2	Water quenching (WQ)	WQ-1453
5		1553	2	AC	N-1553
6		1553	2	WQ	WQ-1553
7	Tempering of steel normalized at 1253 K)	10 33	0.25	AC	N-1253-T-0.25
8		1033	2	AC	N-1253-T-2
9		1033	5	AC	N-1253-T-5

Table 3
Microstructural and microhardness details corresponding to various heat treatments outlined in Table 3.

S. no.	Designation	Microstructure	Microhardness/VHN (load = 100 g)
1	As received	Cold rolled structure	497
2	N-1253	Martensite	429
3	N-1453	Martensite	435
4	N-1553	Martensite + δ ferrite	427
5	N-1253-T-0.25	Tempered martensite	253
6	N-1253-T-2	Ferrite + carbides	207
7	N-1253-T-5	Ferrite + carbides	195

Table 4
Tabulation of heat treatment details adopted for producing different starting microstructure. The $\alpha \rightarrow \gamma$ transformation start (Ac_1) and finish (Ac_3) temperature and the $\gamma \rightarrow \alpha'$ martensitic start (M_S) and finish (M_f) temperatures are also presented together with the corresponding enthalpy change. For M_S measurement, each sample had been taken to 1273 K (1000 °C), held at this temperature for 15 min and this was followed by fast cooling (99 K min^{-1}) to room temperature.

S. no.	Designation	Ac_1 (K)	Ac_3 (K)	$\Delta^\circ H$ for $\alpha \rightarrow \gamma$ transformation (J g^{-1})	M_S (K)	M_f (K)	$\Delta^\circ H$ for $\gamma \rightarrow \alpha'$ martensite transformation (J g^{-1})
1	As received	1103	1139	13	701	610	68
2	N-1253	1107	1140	11	728	621	73
3	N-1453	1105	1146	9	746	689	73
4	N-1553	1102	1145	12	717	675	63
5	N-1253-T-0.25	1106	1136	15	698	611	65
6	N-1253-T-2	1105	1140	13	714	618	63
7	N-1253-T	1108	1141	14	701	607	63

further and polished to regular and nearly identical shapes of mass varying from 50 to 100 ± 0.1 mg. The DSC experiments were performed with *Setaram Setsys* 16® heat-flux type high-temperature differential scanning calorimeter, employing recrystallised alumina crucibles of about 100 μL volume. The description of the equipment and the calibration procedure had been detailed in our previous publication [29,30]. Stated briefly, the experiments were performed under a constant flow (50 ml min^{-1}) of high pure argon. For the estimation of various on-heating transformation temperatures, slow heating rates of 1–5 K min^{-1} were adopted, since higher heating rates resulted in appreciable nonlinear shift of the measured thermal arrest points from their equilibrium values. In order to record the martensitic transformation start (M_S) and finish (M_f) temperatures, a few samples were cooled from 1253 K at 100 K min^{-1}.

For specific heat measurements, a heating rate of 10 K min^{-1} is employed. The adoption of very slow heating rate such as 1 K min^{-1}, for heat capacity measurements is experimentally tedious due to the difficulty in maintaining good thermal stability of the equipment for prolonged time durations. A high heating rate on the other hand is not normally recommended for specific heat study, especially due to the large thermal lag between the sample temperature and that sensed by the non-contact probe [31].

The basic output of a DSC thermogram, namely the heat flow is calibrated in terms of a reference signal obtained using pure iron reference (*Aldrich Chemicals*; with 80 wppm of combined impurity). In the temperature regime that is close to the phase transitions, the recorded temperature lag in case of ferritic steel for a heating rate of 10 K min^{-1} is estimated to be around 2–3 K. The sample mass is kept nearly the same for both the reference iron and steel samples in this case. Fresh samples were used for each run, and multiple runs under identical conditions were performed for calibrating the precision of the measured transformation temperature. The original temperature calibration was performed using recommended high pure melting point standards, namely, Sn, Al, Pb, In and Au. In addition, the measurement of the enthalpy of $\alpha \rightarrow \gamma$ allotropic transformation in pure iron (*Aldrich*, impurities less than 80 wppm) under identical experimental conditions was also carried out. The heat flow rate or specific heat calibration was performed using the literature data on the specific heat of pure iron [32,33]. The measured transformation temperatures are accurate to ±3 K; the transformation enthalpies are accurate to ±5% at 10 K min^{-1}. In Table 4, measured values of transformation temperatures and transformation enthalpy data are listed for different heat treated conditions of RAFM alloy.

2.3.2. Heat capacity measurements

A typical heat capacity measurement using DSC in the continuous heating mode involves recording of at least three consecutive, non-stop experimental runs under identical heating, holding and cooling schedules [34]. In the present study, the experimental schedule consisted of heating the system from room temperature to an initial temperature of 473 K at the rate of 10 K min^{-1} and holding at this temperature for about 15 min. This is required for the attainment of thermal equilibrium of the system before starting any measurement. This is followed by the actual programmed heating, holding and cooling schedules. In the present study, the sample was heated at a steady rate of 10 K min^{-1} to 1473 K, followed by an isothermal hold of about 10 min at this temperature. Subsequently, the sample was cooled to 473 K at 10 K min^{-1} and was allowed a resident time of 15 min at this temperature, before it had been finally cooled again to room temperature. The three basic DSC runs that constitute a C_P measurement are [34]:

(i) the baseline run employing only identical empty crucibles on both sides of the DSC plate,

(ii) the reference or calibration run with the sample crucible containing pure iron of known mass, and

(iii) the sample run with a known mass of ferritic steel loaded onto the sample crucible.

It must be reiterated that all the three runs were performed under identical experimental conditions. In the present study, this scheme was supplemented by an additional baseline run at the end of the above-mentioned three run schedule. This was done in order to ensure or assess the extent of the base line reproducibility at the end of each experimental schedule. A good agreement between the start and finish baselines is suggestive of the stable thermal dynamics prevailing in the DSC sample cradle and the temperature sensor. Besides it also implies that the sample side crucible remains fairly uncontaminated during the course of the experiment. In order to assess the degree of reproducibility of the data, the heat capacity experiments were repeated three times on select samples.

The following formula, based on the method of ratios has been used to calculate C_P, from the three run DSC data [31,34].

$$C_P^S = C_P^R \times (m_R/m_S) \times \{(\mu_s - \mu_b)/(\mu_R - \mu_b)\}. \tag{1}$$

In the above expression, C_P^S and C_P^R represent the specific heat of the sample and the reference whose masses are given by m_S and m_R, respectively. μ_S is the microvolt DSC signal obtained with the sample, μ_R is the corresponding signal obtained with the reference or standard material and μ_b is the baseline signal obtained with empty crucibles.

3. Results

3.1. Microstructural characterization

In Fig. 1, typical optical microstructures of the as received (Fig. 1(a)), normalized (Figs. 1(b)–(d)) and tempered samples (Figs. 1(e)–(g)) are collated. The elongated and deformed grains arising from hot forging treatment are clearly evident in the microstructure of the as received condition (Fig. 1(a)). Figs. 1(b) and (c) show the presence of lath martensite in the steel normalized at 1253 and 1453 K. The prior austenite grain boundaries are fairly well resolved, and their typical dimensions varied from 25 to 40 μm (Figs. 1(b)–(d)). The presence of some δ-ferrite is observed in the steel normalized at 1553 K and this is marked by the arrows in Fig. 1(d). As will be described in detail in the ensuing section, the $M_{23}C_6$ type carbides which are the major ones in 9Cr-type ferritic steels do not undergo a complete dissolution at 1253 K. Moreover,
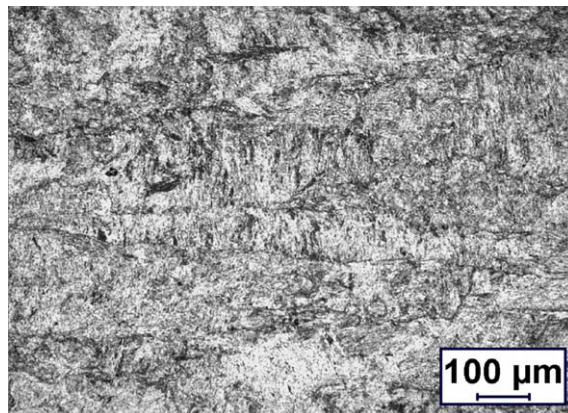

Fig. 1a. Optical micrograph of the RAFM steel in the as received condition showing a highly deformed.
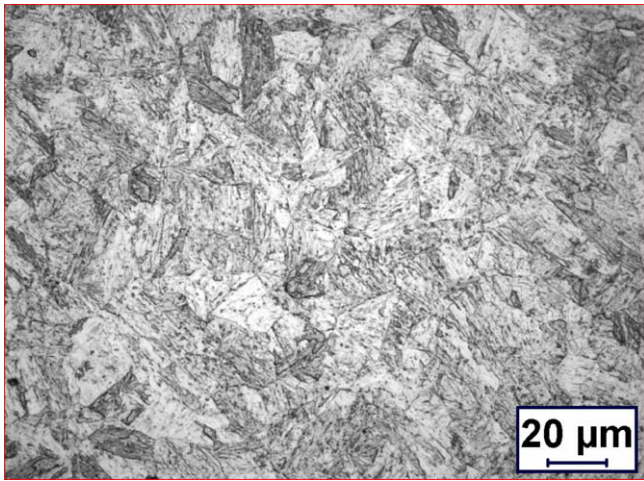
Fig. 1b. Optical micrograph of the sample normalized at 1253 K/2 h, showing martensite structure.

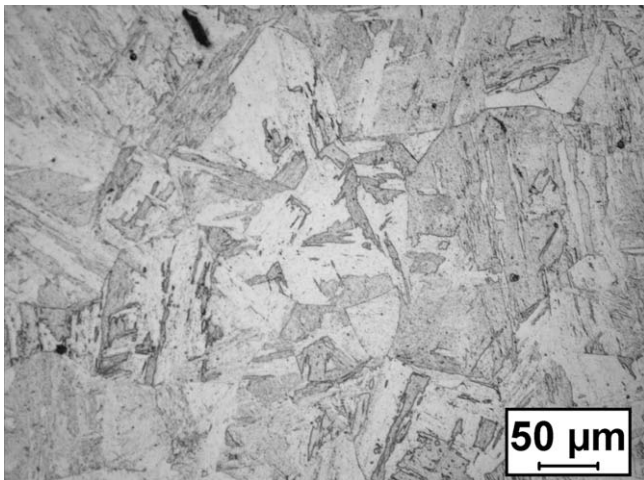**Fig. 1c.** Optical micrograph of the sample normalized at 1453 K showing coarser austenite.

Fig. 1d. Optical micrograph of the sample water quenched from 1553 K showing the presence of some δ-ferrite (marked by arrows) in addition to martensite.

Fig. 1e. Optical micrograph of the sample normalized at 1253 K/2 h, followed by tempering at 1033 K for 30 min.
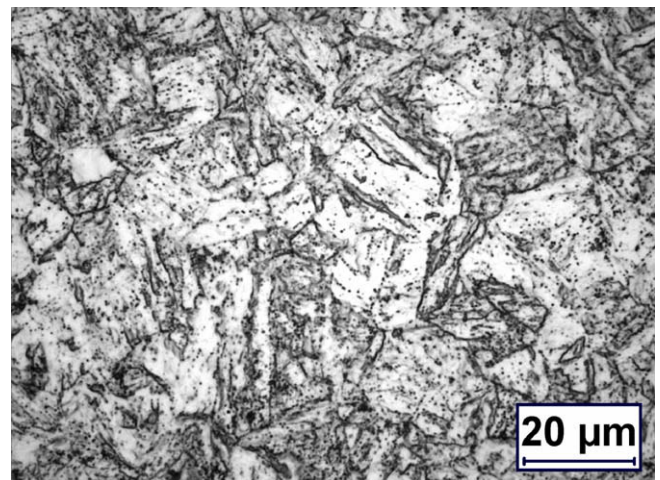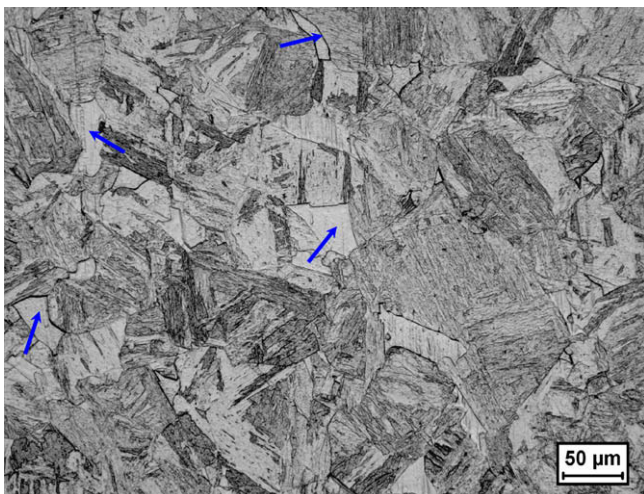

Fig. 1f. Optical micrograph of the sample normalized at 1253 K followed by tempering at 1033 K for 120 min.
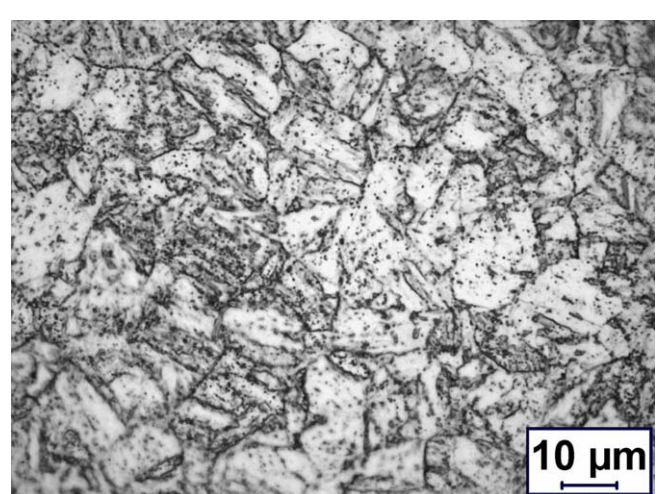

Fig. 1g. Optical micrograph of the sample normalized at 1253 K followed by tempering at 1033 K for 300 min.

Table 5
The on-heating transformation temperatures for RAFM steel as measured by DSC. The heating rate adopted is 5 K min^{-1}. The starting microstructure is derived from the normalization treatment at 1253 K.

Description of phase change	On-heating transformation temperature (K)
α' (martensite) $\rightarrow \alpha$ (ferrite) + M$_{23}$C$_6$	937
Precipitation of M$_{23}$C$_6$ on slow continuous heating	
T_C, Curie temperature	1018
α + MX + M$_{23}$C$_6$ $\rightarrow \alpha + \gamma$ + MX + M$_{23}$C$_6$	1104
Austenite transformation start (Ac_1)	
$\alpha + \gamma$ + MX + M$_{23}$C$_6$ $\rightarrow \gamma$ + MX + M$_{23}$C$_6$	1144
Austenite formation finish (Ac_3)	
γ + MX + M$_{23}$C$_6$ $\rightarrow \gamma$ + MX	1550
Completion of M$_{23}$C$_6$ dissolution	
γ + MX $\rightarrow \delta + \gamma$ + MX	1575
δ-Ferrite formation	
$\delta + \gamma$ + MX $\rightarrow \delta + \gamma$	1681
Completion of MX dissolution	
$\delta + \gamma \rightarrow$ liquid + $\gamma + \delta$	1730
Appearance of liquid	
Liquid + $\gamma + \delta \rightarrow$ liquid + δ	1753
Dissolution of γ-austenite	
Liquid + $\delta \rightarrow$ liquid	1805
Completion of liquid formation	
$\Delta^o H_m$, enthalpy of melting (J g^{-1})	364
$\Delta^o H_{\alpha \rightarrow \gamma}$, enthalpy of $\alpha \rightarrow \gamma$ transformation (J g^{-1})	14

Fig. 2a. Typical DSC thermogram of RAFM steel.

Fig. 2b. The expanded view of the DSC profile around the melting region.

the solvus temperature of the MX type (Ta, V) (CN) mixed carbonitrides is also higher than 1253 K (see, Table 5 for more details). As a result, the presence of some undissolved M$_{23}$C$_6$ and MX type carbides characterize the 1253 K normalized microstructure and these hard dispersed particles exert a strong pinning influence on the growth of austenite grains and thereby yield a fairly stable austenite grain size at these normalization conditions.

Subsequent to normalizing, the tempering treatment at 1033 K resulted in profuse carbide precipitation, both on prior austenite grain boundaries and also inside the grains, decorating thus the lath and sub-grain boundaries of the partially relaxed martensite (Figs. 1(e)–(g)). A longer tempering time of, up to about 5 h in this study, had resulted in carbide coarsening at select locations (Fig. 1(g)). Since the present study is devoted to the enumeration of phase stability and heat capacity related aspects, the subject of microstructural evolution upon thermal treatment is not dealt with in detail in this report.

3.2. DSC studies: on-heating transformation temperatures and transformation enthalpy

In Fig. 2(a), a typical DSC profile obtained during heating (3 K min^{-1}) and cooling (5 K min^{-1}) of a 1253 K normalized sample is illustrated. The presence of various thermal arrest events including the most prominent one, namely melting, is clearly brought out in this figure. In Fig. 2(b), an exclusive, expanded view of the high temperature region, as marked by the ellipse in Fig. 2(a) is portrayed. The actual temperature values of different transformation arrest points are listed in Table 5. Since the enthalpy effects obtained with samples of low mass (75 mg) for various solid state phase changes are rather small, these thermal arrests are determined by taking the derivative signal of the heat flow, in which the occurrence of the inflection points are more clearly delineated. A careful inspection of Fig. 2(a) in the light of the available generic information on the phase stability of 9Cr based steels [5] highlights the following sequence of phase changes that takes place upon slow heating of the RAFM steel. It must also be remarked at this stage that in case of highly hardenable ferritic steels, it is not possible to obtain direct metallographic evidence for the actual phase constitution that exists at high temperatures by performing inter-
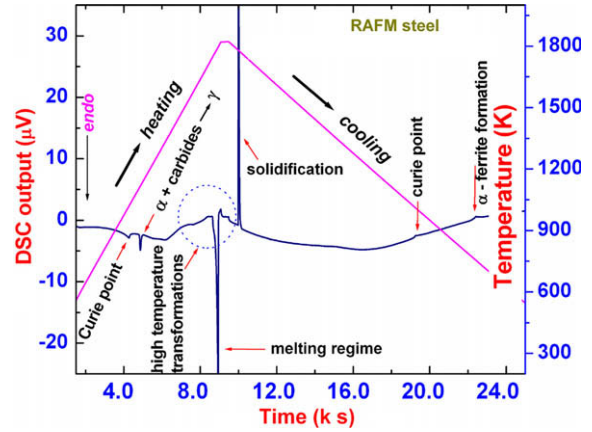
rupted quenching experiments, as this would invariably yield only martensite as the end product. In view of this, we have made use of the available information generated by CALPHAD based *equilibrium* thermodynamic calculations on phase stability in related steels [36,37]. The approximate transformation temperatures provided by these calculations correspond to equilibrium condition, whereas the ones obtained in the present experiment are pertaining to dynamic situation. Nevertheless, the on-heating scans are performed sufficiently slowly so that the knowledge of equilibrium phase stability domains are still useful in indexing the DSC profile.
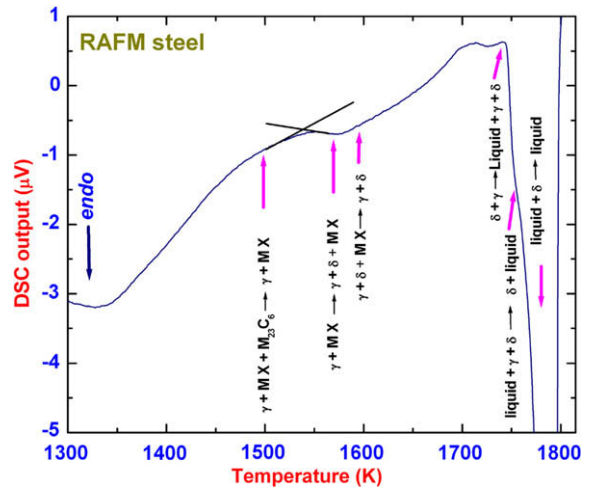
(i) The first transformation on heating is the ferromagnetic to paramagnetic ferrite taking place at T_C, the Curie point of the α-ferrite phase. Depending on the composition, the T_C of 9Cr–1Mo based ferritic steels is found to vary from 1008 to 1023 K [35]. But, owing to the presence of tungsten and tantalum in RAFM steel, a slightly higher value of about 1018 ± 3 K is recorded in this study. The Curie temperature, T_C is found to be more clearly attested during heating than on cooling, as the formation of martensite upon cooling just after the magnetic phase change obscures the sharpness of the magnetic transformation thermal arrest. Note that this martensite transformation during cooling occurs at about 673 K.

(ii) α-Ferrite + M23C6 + MX $\rightarrow \gamma$-austenite + M23C6 + MX (on crossing the Ac_1 temperature); depending on the heating rate, the austenite formation reaches a fair degree of completion at

Ac$_3$ point – the upper critical temperature. It was earlier observed in high chromium steels, that upon reaching Ac$_3$, practically very little dissolution of M23C6 is realized [38], although the *Thermo Calc®* based equilibrium simulations suggest a quite a bit of dissolution (5%) by the time Ac$_3$ is reached [36,37]. This difference is due to the sluggish nature of the dissolution of highly cohesive alloy carbides in highly alloyed ferritic steels, as it involves the transport of substitutional atoms over fairly large distances [38].

(iii) γ + M23C6 + MX $\rightarrow$ γ + MX; (dissolution of M23C6 carbide). Basically, the dissolution of carbide being diffusion mediated one, is a continuous process after Ac$_3$. Since the enthalpy effects associated with this step is rather small due to the small volume fraction of carbides, a sharp DSC peak is not visible for carbide dissolution reaction that is progressing at a slow pace. Instead, this step is generally identified only as a shallow endothermic trough in an otherwise smooth DSC profile [29]. This is observed better only in slow heating rate scans [35].

(iv) γ + MX $\rightarrow$ δ-ferrite + γ + MX; (appearance of high temperature δ-bcc phase).

(v) δ + γ + MX $\rightarrow$ δ + γ; (completion of dissolution of MX phase in γ).

(vi) δ + γ $\rightarrow$ liquid + δ + γ; (appearance of liquid).

(vii) Liquid + δ + γ $\rightarrow$ liquid + δ; (dissolution of γ in liquid).

(viii) Liquid + δ $\rightarrow$ liquid; (completion of melting).

The region covered by the last three thermal arrest events signifies the solidus–liquidus interval in the on-heating phase evolution diagram. In the case of 9–12%Cr–Mo steels with a nominal carbon concentration of about 0.1 wt%, the calculated equilibrium diagram(s) using *Thermo Calc®* software and associated steel database suggests that one may encounter a very small existence domain of the (liquid + δ + γ) three phase field just prior to attaining the (δ + L) two phase region on slow continued heating [36,37]. The presence of a higher austenite stabilizing (Mn + Ni + N) content in typical modified 9Cr–1Mo steel, such as P91 or E911 supports the possibility that a three phase (liquid + δ + γ) equilibrium be realized in principle during slow (1–3 K min^{-1}) heating experiments. The actual attainment is of course dependent on kinetic factors. This aspect has been kept in mind, while annotating the high temperature region of the DSC profiles shown in Fig. 2(b). In Fig. 2(b), it is also interesting to note the subtle features in the nature of the DSC profiles around (liquid + δ) region. The presence of a shoulder like feature in the final melting peak is suggestive of the peritectic dissolution of δ-ferrite in liquid, as for example taking place in dilute Fe–C binary alloys. But this observation needs further careful scrutiny.

It must also be mentioned that for a given DSC instrument and a well prescribed set of experimental conditions, the sharpness or the clearly defined nature of various transformation arrest events is a direct function of the associated enthalpy effect. Unlike the case of $\alpha \rightarrow \gamma$ structural transformation or melting reaction, the other continuously occurring events like the dissolution of M$_{23}$C$_6$ and MX phases are accompanied by only a small change in enthalpy. This is because of the fact that the volume fractions of these phases are small in low carbon 9Cr-steels. Therefore, these changes manifest only as mild, inflections in the base line compensated DSC profile (Fig. 2(b)).

The enthalpy effects associated with $\alpha \rightarrow \gamma$ phase change and melting are given directly in terms of the total area enclosed under the respective peak [34]. The conversion factor required for getting enthalpy in terms of J g^{-1} is obtained from the corresponding signal from pure iron [31]. The measured enthalpy values are listed in the last two rows of Table 5. As for the $\alpha \rightarrow \gamma$ phase change is concerned, there is reasonable agreement between the transformation enthalpy $\Delta^o H^{\alpha \rightarrow \gamma}$ values recorded for RAFM and different P91 compositions. At this point, it must be mentioned that for lower heating rates (1–10 K min^{-1}), the $\alpha \rightarrow \gamma$ transformation peak is found to be diffuse, contributing thereby to a higher degree of uncertainty in the measured peak area and hence enthalpy values. In addition, the low carbon concentration of about 0.09 wt% of the present steel and the fact that solubility of carbon in ferrite is very small, support the argument that it is primarily the substitutionally alloyed ferrite matrix that is getting transformed to austenite in the Ac$_1$–Ac$_3$ intercritical domain; any probable contribution from possible M$_{23}$C$_6$ dissolution in this range is expected to be only marginal.

The measured melting enthalpy values are in the range, 360 J g^{-1}. This value is estimated to be accurate to ±5%, based on similar measurements done on a iron sample with 80 ppm of impurities. Again this estimate is somewhat on the higher side as compared to the values of 240–260 J g^{-1} that are reported for W, Ta free low carbon steels [39]. This must also be viewed with the fact that the effective melting regime or the liquidus–solidus interval is rather large in high alloy ferritic steels compared to the low alloyed ones and hence the melting peak encompasses a larger area.

3.3. Specific heat data

In Fig. 3(a), the measured variations in specific heat C_P with temperature for the RAFM steel in the as received and in different normalized conditions are compared. These curves are typical of untempered martensites. The presence of sharp peaks arising from magnetic and $\alpha \rightarrow \gamma$ transformations are clearly evident in all the
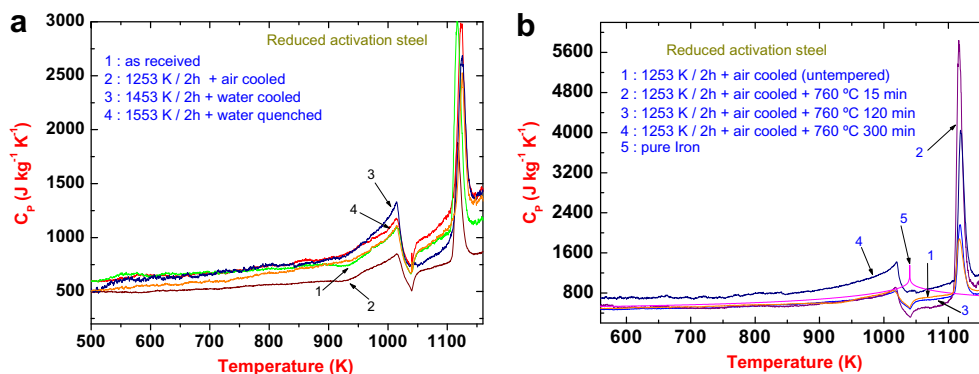

Fig. 3. (a) The temperature variation of specific heat for RAFM steel in different normalized conditions. (b) In different tempered conditions. Note that in (a), the y-axis scale is compressed in order to bring out the very small differences among different martensites.

Table 6
Listing of fitting parameters of the measured specific heat data to expression given by Eq. (2). The T_C used in fitting is 1015 K for all samples. The overall temperature range of the data chosen for fitting is 480–1020 K, except for three cases, for which the presence of wiggles in the low temperature region adversely affected the quality of the fit. Hence a slightly restricted temperature range is adopted for these three cases.

$C_P/\text{J Kg}^{-1}\text{ K}^{-1} = AT + BT^2 + CT^3 + D/T + E\ \ln\{abs(T - T_C/T_C)\}$					
Steel designation	A (J kg^{-1})	B (J K kg^{-1})	C (J K^2 kg^{-1})	D (J kg^{-1} K^{-2})	E (J kg^{-1} K^{-1})	R^2
As received	7.49 ± 0.19	−0.012 ± 0.0004	$6.005 \times 10^{-6} \pm 1.87 \times 10^{-7}$	−282008.08 ± 18204.70	−49990.18 ± 1603.45	0.96
N-1253 (fitted from 502 K)	3.62 ± 0.12	−0.006 ± 0.00002	$2.92 \times 10^{-6} \pm 1.22 \times 10^{-7}$	−35217.63 ± 11363.64	−33741.84 ± 1161.93	0.97
WQ-1453 (fitted from 510 K)	10.39 ± 0.28	−0.017 ± 0.0005	$8.83 \times 10^{-6} \pm 2.75 \times 10^{-7}$	−539099.68 ± 27141.32	−59337.22 ± 2292.46	0.97
WQ-1553	5.38 ± 0.13	−0.009 ± 0.0002	$4.81 \times 10^{-6} \pm 1.33 \times 10^{-7}$	−132584.48 ± 12371.99	−32960.89 ± 1261.34	0.99
N-1253-T-0.25	2.59 ± 0.05	−0.004 ± 0.0001	$2.28 \times 10^{-6} \pm 25.04 \times 10^{-8}$	13871.21 ± 4741.66	−21122.24 ± 463.56	0.99
N-1253-T-2 (fitted from 665 K)	10.64 ± 0.61	−0.018 ± 0.001	$8.57 \times 10^{-6} \pm 4.58 \times 10^{-7}$	−760670.77 ± 69469.79	−30653.01 ± 1298.51	0.99
N-1253-T-5	10.30 ± 0.15	−0.018 ± 0.0003	$9.70 \times 10^{-6} \pm 1.54 \times 10^{-7}$	−467265.84 ± 14137.71	−39011.25 ± 1454.94	0.99

curves. It is also observed that no significant difference in the specific heat characteristics of different martensitic microstructures that are obtained by fast cooling from different austenitisation temperatures is noticed. This is understandable from the fact that this steel is fully hardenable upon cooling from austenite regime. As compared to higher austenitizing temperatures, the 1253 K normalized sample contained a higher fraction of undissolved carbides, and since the C_P of $M_{23}C_6$ + MX carbides is less than that of carbon lean α-ferrite (solubility of carbon in bcc-iron is less), this sample shows a comparatively lower heat capacity among different normalized microstructures.

In Fig. 3(b), the C_P–T data are compared for tempered samples that had seen three different tempering durations (15, 120 and 300 min) at 1033 K. For comparison, the data on one untempered sample (1253 K + air cooling) are also co-plotted here. In accordance with our previous findings on tempered and aged 9Cr–1Mo steels [31,39], the heat capacity is expected to show a mild increase with tempering time and temperature and this is attributed to the reduction in the stored energy of martensite, following substructure reorganization upon thermal activation [31]. In the case of W-added RAFM steel, a similar trend is observed, although in a subdued manner. This is because the presence of W and Ta, the two comparatively more cohesive substitutes for Mo slows down the rate of relaxation of martensite upon tempering. The enhanced cohesive character of the RAFM steel due to W addition may be inferred from the fact that the replacement of Mo by W enhances marginally the solid solution strengthening and thereby improves the creep properties as well [28]. Besides, the coarsening rates of carbides are also slowed down in W added steel due to reduced diffusion rates [40]. The influence of W addition is implicitly borne out in the present experimental findings in that, only for the 5 h tempered sample, the measured C_P curve (curve 4 in Fig. 3(b)) is placed distinctly above the corresponding untempered one (curve 1 in Fig. 3(b)). Note that the y-axis scales are slightly different for these two C_P–T plots, which drive home the point that tempering serves to increase the heat capacity somewhat in W added steel. However, a resolution of this issue in more quantitative terms, calls for further comparative studies with long term thermally aged samples, which are expected to have reached full thermodynamic equilibrium. These issues are scheduled for future study.

The experimental specific heat versus temperature data in the α-ferrite region are fitted to the following empirical functional representation:

$$C_P/\text{J kg}^{-1}\text{ K}^{-1} = aT + bT^2 + CT^3 + D/T + E\ \ln\{abs(T - T_C/T_C)\}. \tag{2}$$

The last term on the right hand side of the above expression represents the magnetic contribution to the total C_P. Although more sophisticated expressions are used in literature for representing ΔC_P^{mag} [32], we have chosen a simple functional representation here as this captures fairly adequately the experimental scenario. The values of fit parameters in Eq. (2) are listed in Table 6.

4. Discussion

At the outset, it must be mentioned that although the physical metallurgy of advanced 9Cr-steels is replete with many investigations devoted to the elucidation of microstructural development upon thermal treatment [1–27], there are not many calorimetry based studies focused on the energetics and kinetics related aspects of phase changes [29,31,39]. In this regard, the present study attempts to shed some light on the phase transformation sequence that follows as a result of continuous heating of normalized and tempered RAFM steel. It is believed that the findings of this study, especially the phase transformation temperatures and their enthalpies offer data that are useful in a simulation study of diffusional phase transformation kinetics.
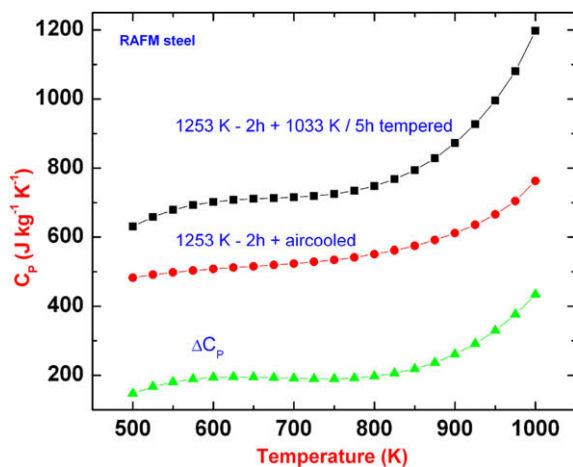
The phase transformation temperatures that are obtained in this study are in general agreement with the values found for general 9Cr–1Mo based low carbon steels [39]. In case of RAFM steel, the values of Ac_1 and Ac_3 temperatures for different tempered microstructures are very similar; in other words no appreciable microstructure sensitivity of transformation temperatures *per se* is apparent from this study. But in terms of absolute values, it is noted that they are slightly higher than the corresponding values obtained for tungsten and tantalum free plain 9Cr–1Mo steels [29,39]. The clear qualitative reason for this is that the addition of tungsten and tantalum, enhances the stability of the α-ferrite phase. For the same reason, it is also expected that the addition of tungsten will exert a significant influence on austenite formation kinetics upon high temperature homogenization step, since W and Ta additions will serve to decrease the diffusivity in ferrite phase, as for example they do in the bcc phase of iron [40].

Akin to the diffusional transformation onset temperature, the martensite start (M_s) and finish (M_f) temperatures recorded upon cooling for the RAFM steel are found to be slightly higher than that recorded for conventional 9Cr–1Mo steels [29,39]. More importantly, they seem to be influenced by the microstructure (presence of carbides and austenite grain size) prevailing at the austenitising conditions. At about 1253 K for example, the complete dissolution of the carbide phase is not realized for reasons that are already mentioned before; and the retention of a large fraction of undissolved carbides results in an austenite phase that is not quite rich in carbon. So the M_S of this *carbon lean* austenite is expected to be somewhat higher than the *carbon rich* austenite that would have been obtained under a relatively higher austenitising temperature and prolonged annealing durations. As an added influence, the presence of some coarse $M_{23}C_6$ and fine MX particles exert a pinning effect on the advancement of martensitic transformation front. In view of this later effect, a higher austenitizing temperature (1453–1553 K) would obviously result in more extensive dissolution of $M_{23}C_6$ carbides, which would in turn serve to decrease M_S. Further, systematic studies on the effect of processing variables on M_S are currently under progress.

At this stage, it may be mentioned in general terms that a full fledged explanation of the effect of W, Ta addition on the phase

Table 7
A comparison of C_P of martensitie with that of tempered martensite.

Temperature (K)	C_P martensite (J kg^{-1} K^{-1})	C_P tempered martensite (J kg^{-1} K^{-1})
500	483	631
525	491	659
550	498	679
575	504	693
600	508	702
625	512	708
650	516	711
675	520	713
700	524	715
725	529	719
750	535	725
775	542	734
800	551	748
825	562	768
850	575	794
875	591	828
900	611	872
925	636	927
950	666	995
975	704	1081
1000	763	1197

Fig. 4. The C_P of martensite, tempered martensite and their difference with temperature are plotted.

transformation characteristics of RAFM steels calls for the generation of data on a range of compositions with varying W and Ta contents. This effort must also be supplemented by a corresponding research on phase stability estimation in terms of CALPHAD methodology. The present paper, being exclusively dedicated to the generation of reliable data on one select RAFM composition, does not attempt to provide an answer on a fundamental note. Nevertheless, an attempt has been made to qualitatively explain the data using available literature information. Clearly more work is required to shed further insight on this crucial issue.

In Table 7, the difference in C_P (ΔC_P) between the martensitic microstructure and the one tempered for 5 h is tabulated at select temperature intervals. As can be seen, the heat capacity of the tempered sample is higher than that of the virgin martensite; but what is remarkable about this observation is that this difference is becoming significant at high temperatures ($T \geqslant 923$–973 K), where the thermally activated relaxation processes are poised to become active. This aspect is also nicely brought out in Fig. 4, wherein the rise in ΔC_P is rather steep at high temperatures. One important point that must be kept in mind while interpreting this ΔC_P, is that the martensite sample had been undergoing concurrent relaxation

even as the measurement of its C_P was going on. In this sense, what is measured in the present study is not the true or exact contribution to C_P arising from the relaxation processes operating in martensite; but it is expected that at 10 K min^{-1} heating rate with a minimal prior hold at 373 K for attaining thermal equilibrium, the difference in C_P estimated in this study is somewhat reflective of the contribution arising from the overall relaxation process operating in martensite.

5. Conclusions

(1) A differential scanning calorimetry determination of on-heating phase transformation temperatures and specific heat have been made for normalized and tempered reduced activation ferritic–martensitic steels.
(2) The α-ferrite + M$_{23}$C$_6$ + MX $\rightarrow$ γ-austenite + M$_{23}$C$_6$ + MX, transformation start and finish temperatures namely Ac_1, and Ac_3, are found to be 1104 and 1144 K, respectively.
(3) The martensite transformation temperatures are mildly sensitive to the starting microstructure. For the steel normalized at 1253 K and tempered for 120 min at 1033 K, the martensitic start (M_S) and finish (M_f) temperatures are of the order of 714 and 618 K, respectively.
(4) The heat capacity of normalized and tempered microstructures at room temperature varies from 500 to 550 J kg^{-1} K^{-1}. However, the difference between them is found to be a strong function of temperature, with the C_P of tempered microstructure turning out to be larger than the untempered martensite by about 300 J kg^{-1} K^{-1} at 1000 K.

References

[1] T. Fujita, ISIJ Int. 32 (1992) 175.
[2] Ulrich E. Klotz, Christian Solenthaler, D.J. Uggowitzer, Mater. Sci. Eng. A476 (2008) 186.
[3] R.L. Klueh, Curr. Opin. Solid State Mater. Sci. 8 (2004) 239.
[4] R.L. Klueh, K. Ehrlich, F. Abe, J. Nucl. Mater. 191–194 (1992) 116.
[5] J. Orr, F.R. Beckitt, G.D. Fawkes, in: S.F. Pugh, E.A. Little (Eds.), Ferritic Steels for Fast Reactor Steam Generators, BNES, London, 1978, p. 91.
[6] A.G. Ioltukhovsky, V.P. Kondratev, M.V. Leont'eva Smirnova, S.N. Votinov, V.K. Shamardin, A.V. Povstyanko, T.M. Bulanova, J. Nucl. Mater. 233–237 (1996) 299.
[7] R.L. Klueh, J. Nucl. Mater. 378 (2008) 159.
[8] R.L. Klueh, P.J. Maziasz, J. Nucl. Mater. 155–157 (1988) 602.
[9] M. Tamura, H. Hayakawa, A. Yoshitake, A. Hishinuma, T. Kondo, J. Nucl. Mater. 155–157 (1988) 620.
[10] A. Kohyama, A. Hishinuma, D.S. Gelles, J. Nucl. Mater. 233–237 (1996) 138.
[11] P. Fernandez, A.M. Lancha, J. Lapena, M. Hernandez-Mayoral, Fus. Eng. Des. 58&59 (2001) 787.
[12] A. Danon, C. Servant, J. Nucl. Mater. 321 (2003) 8.
[13] Vaclav Foldyna, J. Purmensky, Z. Kuban, ISIJ Int. 41 (2001) S81.
[14] K. Sawada, M. Taneike, K. Kimura, F. Abe, Mater. Sci. Technol. 19 (2003) 739.
[15] M. Tamura, H. Kusuyama, K. Shinozuka, H. Esaka, ISIJ Int. 47 (2007) 317.
[16] K. Yamada, M. Igarashi, S. Muneki, F. Abe, ISIJ Int. 42 (2002) 779.
[17] F. Abe, Mater. Sci. Eng. A319–321 (2001) 770.
[18] M. Tamura, Y. Haruguchi, M. Yamashita, Y. Nagaoka, K. Ohinata, K. Phnishi, E. Itoh, K. Shinozuka, H. Esaka, ISIJ Int. 46 (2006) 1693.
[19] K. Asakura, Y. Yamashita, T. Yamada, K. Shibata, ISIJ Int. 30 (1990) 937.
[20] A. Zielinska-Lipiec, A. Czyrska-Filemonowicz, P.J. Ennis, O. Wachter, J. Mater. Process. Technol. 64 (1997) 397.
[21] M. Tamura, H. Kusuyama, K. Shinozuka, H. Esaka, ISIJ Int. 47 (2007) 317.
[22] Y. Tsuchida, K. Okamoto, Y. Tokunaka, ISIJ Int. 35 (1995) 317.
[23] F. Abe, T. Horiuchi, M. Taneike, K. Sawada, Mater. Sci. Eng. A378 (2004) 299.

[24] F. Abe, T. Noda, H. Araki, S. Nakazawa, J. Nucl. Mater. 179–181 (1991) 663.
[25] S.G. Hong, W.B. Lee, C.G. Park, J. Nucl. Mater. 288 (2001) 202.
[26] P. Fernandez, M. Hernandez-Mayotal, J. Lapena, A.M. Lancha, G. de Diego, Mater. Sci. Technol. 18 (2002) 1353.
[27] T. Horiuchi, M. Igarashi, F. Abe, ISIJ Int. 42 (2002) S67.
[28] Kouichi Maruyama, Kota Sawada, Jun-ichi Koike, ISIJ Int. 41 (2001) 641.
[29] S. Raju, B. Jeyaganesh, A. Banerjee, E. Mohandas, Mater. Sci. Eng. A465 (2007) 29.
[30] S. Raju, N.S. Arun Kumar, B. Jeyaganesh, E. Mohandas, U. Kamachi Mudali, J. Alloys Compd. 440 (2007) 173.
[31] B. Jeyaganesh, S. Raju, E. Mohandas, S. Murugesan, M. Vijayalakshmi, Int. J. Thermophys., in press.
[32] Q. Chen, B. Sundman, J. Phase Equilib. 22 (2001) 631.
[33] P.D. Desai, J. Phys. Chem. Ref. Data 15 (1986) 967.
[34] M.J. Richardson, in: K.D. Maglic, A. Cezairliyan, V.E. Peletsky (Eds.), Compendium of Thermophysical Property Measurement Techniques, vol. 2, Plenum, New York, 1992, p. 519.
[35] S. Raju, unpublished research, 2008.
[36] A. Danon, C. Servant, ISIJ Int. 45 (2005) 903.
[37] A. Kroupa, J. Havrankova, M. Coufalava, M. Svoboda, J. Vrestal, J. Phase Equilib. 22 (2001) 312.
[38] U.R. Lenel, R.W.K. Honeycombe, Met. Sci. 18 (1984) 201.
[39] B. Jeyaganesh, S. Raju, E. Mohandas, M. Vijayalakshmi, Defect Diffus. Forum 279 (2008) 85.
[40] J. Cermak, J. Ruzickova, A. Pokorna, Scr. Met. Mater. 32 (1995) 1631.